Applied Catalysis B: Environment and Energy 379 (2025) 125708

Contents lists available at ScienceDirect

Applied Catalysis B: Environment and Energy

journal homepage: www.elsevier.com/locate/apcatb

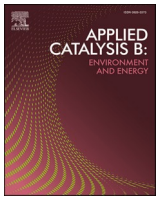

# Asymmetrically coordinated Ru-O site facilitates $H_2$ heterolytic cleavage for efficient green reductive amination of octanol to octylamine: A mechanistic investigation

Zhexi Gao [a,1], Qian Wang [a,b,1], Haoran Ma [a], Huifang Wu [a], Richard Lewis [c], Dave Willock [c], Ouardia Akdim [c,*], Junting Feng [a,b,**], Graham J. Hutchings [c,*]

[a] State Key Laboratory of Chemical Resource Engineering, Beijing Engineering Center for Hierarchical Catalysts, Beijing University of Chemical Technology, Beijing 100029, China

[b] Quzhou Institute for Innovation in Resource Chemical Engineering, Quzhou 324000, China

[c] Max Planck-Cardiff Centre on the Fundamentals of Heterogeneous Catalysis FUNCAT, Cardiff Catalysis Institute, School of Chemistry, Cardiff University, Translational Research Hub, Cardiff CF24 4HQ, United Kingdom

ARTICLE INFO

*Keywords:*
Asymmetric coordination
Heterogeneous catalysis
$H_2$ heterolytic cleavage
Reductive amination

ABSTRACT

The catalytic reductive amination of octanol exhibits a promising and environmentally friendly pathway for the synthesis of octylamine, a compound with significant applications in the bulk and fine chemical sectors. However, the complexity of this reaction lies in the necessity of a catalyst that can simultaneously facilitate both the dehydrogenation and hydrogenation steps, occurring during the reaction. Herein, we have addressed this issue by designing a $Ru@TiO_x/Mg_9Al_6Ti_6O_x$ catalyst with Ru-Ru and Ru-O asymmetric coordination structure that leads to 100 % octanol conversion, 94.6 % octylamine selectivity and a turn over frequency of 73.41 $h^{-1}$, while maintaining the same activity for 4 consecutive cycles. Those performances, firmly positioning our catalyst among the most advanced and efficient catalysts reported to date. Using EXAFS, *in situ* FTIR, kinetic isotope experiments, and DFT calculations, we proposed a mechanism where Ru-O coordination structure promote the heterolytic cleavage of $H_2$, producing highly active $H^+/H^-$ species that can achieve efficient hydrogenation without hindering the dehydrogenation process. This work not only provides a promising catalyst for industrial application, but presents a valuable catalyst design strategy that involves complex tandem dehydrogenation/hydrogenation reactions.

## 1. Introduction

Aliphatic amines, synthesized from fatty acids, olefins, or alcohols, play a crucial role as building blocks in organic synthesis, serving as intermediates across both bulk and fine chemical industries to create a wide array of complex molecules including polymers, dyes, pharmaceuticals, agrochemicals, surfactants, and biologically active substances. Their versatility stems from the nucleophilic nature of the nitrogen atom, which readily participates in various reactions [1–4]. Among those, octylamine, $CH_3(CH_2)_7NH_2$ is used, *inter alia,* as a chiral resolving agent for pharmaceutical drugs such as ibuprofen and naproxen [5–9]. The octylamine global market evaluated at USD 1.5 billion in 2018, is projected to have a steady growth, reaching an estimated USD 2.1 billion by 2030 [10]. Unfortunately, existing alkylamine production methods often depend on hazardous reagents such as HCN or produce harmful by-products like hydrochloric acid HCl, posing significant environmental concerns and hindering sustainable implementation [11–18]. Among the emerging green alternatives, the reductive amination of 1-octanol to 1-octylamine stands out as particularly promising [19,20]. This method involves a hydrogen-assisted amination reaction, which is highly valuable in fine chemistry. This process facilitates the interconversion of unsaturated and saturated chemical bonds, producing water as the only by-product. Furthermore, the low cost of the raw materials and the minimal production of the by-products make this approach

* Corresponding authors.
** Corresponding author at: State Key Laboratory of Chemical Resource Engineering, Beijing Engineering Center for Hierarchical Catalysts, Beijing University of Chemical Technology, Beijing 100029, China.
*E-mail addresses:* akdimo@cardiff.ac.uk (O. Akdim), fengjt@mail.buct.edu.cn (J. Feng), Hutch@cardiff.ac.uk (G.J. Hutchings).
[1] These two authors contributed equally to this work. They are cofirst authors.

https://doi.org/10.1016/j.apcatb.2025.125708
Received 7 May 2025; Received in revised form 3 July 2025; Accepted 16 July 2025
Available online 17 July 2025

highly promising for large-scale applications. However, the challenge lies in achieving a balance between selectivity and activity, which requires the rational design of bifunctional catalysts. Typically, reductive amination of 1-octanol involves three sequential steps: (1) alcohol dehydrogenation to aldehyde, (2) aldehyde amination to imine and (3) imine hydrogenation to 1-octylamine (Scheme 1).

Specifically, the dehydrogenation of the alcohol to the aldehyde acts as a switch for the entire reaction. According to Le Chatelier's principle, the presence of massive exogenous hydrogen is detrimental, as it hinders the forward progression of the reaction. Although the aldehyde amination to imine process does not require a catalyst, the catalytic hydrogenation of the imine intermediate is crucial for ensuring reaction selectivity. Indeed, when the imine accumulates in large quantities, it can undergo self-condensation or can react with 1-octylamine leading to the formation of secondary amines such as dioctylamine [19]. Therefore, once formed, the imine must be rapidly hydrogenated to the targeted octylamine, to prevent its accumulation in the system. This necessitates a substantial amount of exogenous hydrogen to drive the hydrogenation process forward. Consequently, a typical seesaw-like dynamic arises between dehydrogenation and hydrogenation, resulting in suboptimal overall catalytic performance. Therefore, the precise control of hydrogen over its availability and reactivity is essential and offers a transformative solution to the limitations currently observed in this reaction.

The activation of hydrogen in such reactions can occur through two main modes, *i.e.,* homolytic or heterolytic cleavage [21–24]. The homolytic activation is the more prevalent mode, yielding to the formation of two $H^{\cdot}$ radicals, with equal charges. In contrast, the heterolytic activation splits hydrogen into $H^{+}$ and $H^{-}$, resulting in uneven charges distribution and distinct reactivity, particularly beneficial for hydrogenating polar unsaturated groups (*e.g.,* C═O and C═N) [23–25]. Thus, altering the hydrogen activation mode offers a potential solution to the seesaw mechanism between dehydrogenation and hydrogenation processes. In this strategy, using high exogenous hydrogen pressure to drive hydrogenation process is avoided, therefore dehydrogenation process is not affected. Meanwhile, due to the outstanding reactivity of both $H^{+}$ and $H^{-}$ species the hydrogenation of the imine is facilitated.

The heterolytic activation of $H_2$ is primarily influenced by the asymmetric coordination structure. For instance, M-B (metal-other atoms) active site type, due to their differing chemical properties, can promote hetero-cleavage of $H_2$ [21,22]. To successfully design the desired asymmetric coordination structure, the construction of an interface between two different phases is crucial. Layered double hydroxides (LDHs) are a class of advanced catalytic platform materials that are well-suited for precisely designing interfacial and asymmetric coordination structures[13,26,27]. LDHs are typical two-dimensional materials with general chemical formula $M^{II}_{1-x}M^{III}_{x}(OH)_2(A^{n-})_{x/n}.yH_2O$, where $M^{II}/M^{III}$ are divalent/trivalent metallic cations[28–30]. The compositional flexibility and structural tunability of LDHs materials enable the strategic introduction of the required elements into the layered structure. This allows the construction of highly customized catalytic interfaces and asymmetric coordination environments. The ability to precisely control the chemical composition and spatial arrangement of the active sites within the LDHs framework is a key advantage of this material platform. Moreover, the unique thermal topological transformation process associated with LDHs can drive the migration of reducible elements from the layer to the surface. During heat treatments, those mobile species can selectively decorate the supported metal nanoparticles and can enhance the catalytic performance [26,27,29]. This thermal transformation process provides an additional lever for tailoring the structure and composition of the active sites at the nanoscale.

Herein, Ru was selected for its well-established efficiency for amination reactions [31–35]. We then introduced different ratios of the reducible species $Ti^{4+}$, into a MgAl-LDHs framework as the asymmetric coordination structure building block. By judiciously selecting the active metal (Ru) and strategically incorporating the reducible $Ti^{4+}$ species into the LDHs structure, we designed a $Ru@TiO_x/Mg_9Al_6Ti_6O_x$ catalyst with Ru-Ru and Ru-O asymmetric coordination structure that leads to 100 % 1-octanol conversion, 94 % 1-octylamine selectivity, a TOF of 73.41 $h^{-1}$, stable for 4 consecutive cycles.

## 2. Experimental section

### 2.1. Materials

$Mg(NO_3)_2{\cdot}6\ H_2O$, $Al(NO_3)_3{\cdot}9\ H_2O$, $TiCl_4$, NaOH, and $NaNO_3$ were purchased from Sinopharm Chemical Reagent Co., Ltd. 1-octanol, biphenyl, o-xylene, $RuCl_3{\cdot}3\ H_2O$ and MgO were purchased from Macklin. The above chemicals were analytical grade and used as received without further purification. Gaseous chemicals including $H_2$, $N_2$, $D_2$, CO and Ar were bought from Beijing Air Liquid Company. The purity of the gaseous chemicals were all 99.999 %.

### 2.2. Synthesis methods of MgAlTi-LDHs

The synthesis procedure was carried out following the same protocol as described in our previous work [13].

MgAlTi-LDHs with different metal ratios were synthesized by dissolving the required amounts of metal salts ($Mg(NO_3)_3{\cdot}6\ H_2O$, Al

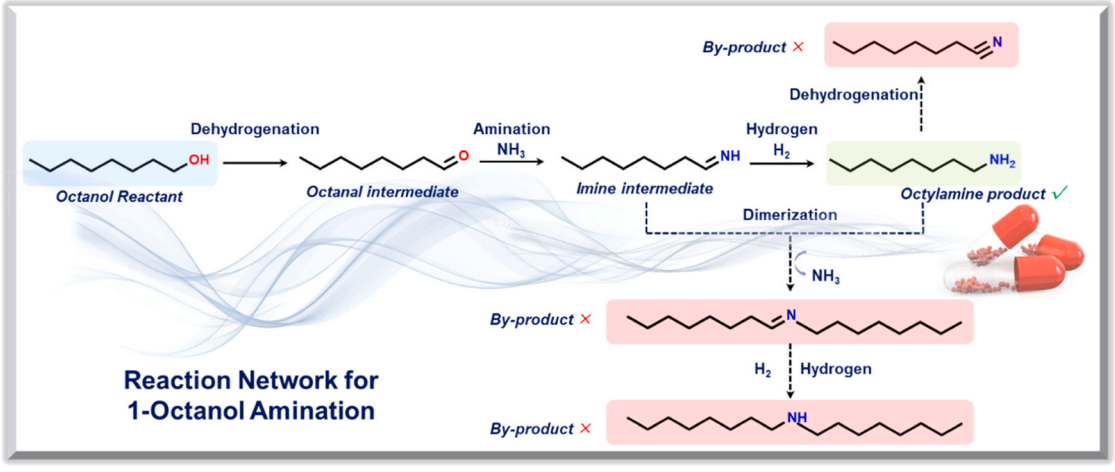


**Scheme 1.** 1-octanol reductive amination pathways.

$(NO_3)_3{\cdot}9\ H_2O$, $TiCl_4$) in 60 mL deionized water to form Solution A. For example, in the case of $Mg_9Al_6Ti_9$-LDHs, 9 mmol of $Mg(NO_3)_3{\cdot}6\ H_2O$, 6 mmol of $Al(NO_3)_3{\cdot}9\ H_2O$, and 9 mmol of $TiCl_4$ were used, while for $Mg_9Al_6Ti_6$-LDHs, 6 mmol of $TiCl_4$ was used, and for $Mg_9Al_6Ti_3$-LDHs, only 3 mmol of $TiCl_4$ was used. In Solution B, NaOH and $NaNO_3$ were dissolved in 60 mL of deionized water. Both solutions were then added dropwise into a 250 mL flask under continuous stirring. The mixture was heated in a water bath at 80 °C for 8 h to allow crystallization. Afterward, the resulting precipitate was centrifuged, washed thoroughly with deionized water, and dried at 90 °C for 12 h. The final products, each with different metal ratios, were labeled according to their respective compositions, such as $Mg_9Al_6Ti_9$-LDHs, $Mg_9Al_6Ti_6$-LDHs, and $Mg_9Al_6Ti_3$-LDHs.

### 2.3. Catalysts preparation

Ru-based catalysts were prepared using a wet impregnation method, as established in our prior study [13]. Briefly, 1.00 g of LDHs or MgO powder were dispersed in 10 mL of deionized water under vigorous stirring, followed by the addition of $RuCl_3$ solution. The mixture was heated to 90 °C until complete evaporation of the solvent, and then thermally reduced under a $H_2/N_2$ (1:9) mixture at 450 °C, depending on the precursor composition. According to the amount of Ti introduced within the LDHs structure the catalysts were named $Ru/Mg_9Al_6O_x$, $Ru@TiO_x/Mg_9Al_6Ti_3O_x$, $Ru@TiO_x/Mg_9Al_6Ti_6O_x$ and $Ru@TiO_x/Mg_9Al_6Ti_9O_x$. The catalysts using MgO as support was named Ru/MgO.

### 2.4. Sample Characterizations

X-Ray diffraction (XRD) analysis was conducted on the samples using a Shimadzu XRD-6000 diffractometer with Cu Kα radiation (λ = 0.154 nm) to investigate the crystal structures. The scanning angle was set between 3° and 80° with a scan speed of 10°/min. For microstructural characterization, we employed both the Thermo Scientific Themis Z and JEOL JEM-2100F instruments. To analyze the surface properties, CO adsorption (CO-IR) FT-IR spectra were obtained using a Bruker Tensor 27 spectrometer equipped with a high-sensitivity MCT detector. The resolution was maintained at 4 $cm^{-1}$, and the gas flow rate was set at 20 mL/min. Then, 20 mg of sample was pressed into 10 mm diameter self-supporting disks and placed into the FT-IR cell. Prior to measurement, the samples were treated under a pure argon flow (20 mL/min) at 120 °C for 1 h to remove any impurities or residual moisture. Subsequently, CO was introduced as the probe molecule at 30 °C for 30 min until adsorption reached saturation. The gas flow was then switched to argon to purge the physically adsorbed CO, and the final spectra were recorded.

Density functional theory (DFT) calculations were conducted using the Vienna Ab Initio Package (VASP), applying the generalized gradient approximation (GGA) with the Perdew, Burke, and Enzerhof (PBE) functional. The projected augmented wave (PAW) potentials were utilized for describing the ionic cores, while the valence electrons were represented using a plane wave basis set with a cutoff energy of 450 eV. Partial occupancy of the Kohn-Sham orbitals was permitted using the Gaussian smearing technique, set at a width of 0.05 eV. Energy self-consistency was achieved when the energy change dropped below $10^{-6}$ eV. A geometry optimization was deemed convergent when the force difference was smaller than 0.03 eV/Å. For modeling dispersion interactions, the DFT-D3 method by Grimme was employed. To determine the migration barriers for hydrogen ions (H ions), the Climbing Image-Nudged Elastic Band (CI-NEB) approach was applied. The adsorption energy ($E_{ads}$) was computed using the following relation:

$$E_{ads} = E_{ad/sub} - E_{ad-Esub},$$

where $E_{ad/sub}$, $E_{ad}$, and $E_{sub}$ are the total energies of the optimized adsorbate/substrate system, the adsorbate in the gas phase, and the clean substrate, respectively [36–41].

### 2.5. Catalytic performance tests

The catalytic tests were performed in a 25 mL stainless steel autoclave equipped with a magnetic stirrer. In a typical procedure, the autoclave was loaded with 250 mg catalyst, 2 mmol 1-octanol and 15 mL o-xylene, purged beforehand by $NH_3$ (99.999 %) for 10 times and then charged with 0.55 MPa $NH_3$. Subsequently, the reactor was charged with $H_2$, bringing the total pressure to 0.95 MPa and heated up to 180 °C. The reaction was then conducted at 180 °C under a stirring speed of 800 rpm. Samplings of the liquid mixture, during the reaction, were performed every 3 h for analysis. The liquid products were separated from the catalyst by centrifugation, then mixed with biphenyl as internal standard and were analyzed with an Agilent gas chromatograph (7890B) equipped with an FID detector and HP-5 capillary column. Products identification was carried out by GC-MS (Agilent 7890B-5977A). The conversion, selectivity and yield were calculated using the following equations:

$$\text{Conversion}(\%) = \frac{\text{1-octanol converted(mol)}}{\text{initial 1-octanol(mol)}} \times 100\%$$

$$\text{Selectivity}(\%) = \frac{\text{product formed(mol)}}{\text{converted 1-octanol(mol)}} \times 100\%$$

$$\text{Yield}(\%) = \frac{\text{carbon atoms in the products}}{\text{carbon atoms of 1-octanol added into reactor}} \times 100\%$$

To rigorously assess the reusability of the best catalyst, we selected a 3-hour reaction time to ensure a low octylamine yield and more stringent testing conditions. The catalyst was recovered by centrifugation from the reaction mixture, washed with o-xylene for 3 times and reused for the next cycle.

## 3. Results and discussion

### 3.1. Catalysts physicochemical properties

Ru supported on $Mg_9Al_6$-LDHs with varying Ti content and without Ti, were synthesized and named $Ru@TiO_x/Mg_9Al_6Ti_3O_x$, $Ru@TiO_x/Mg_9Al_6Ti_6O_x$ $Ru@TiO_x/Mg_9Al_6Ti_9O_x$ and $Ru/Mg_9Al_6O_x$ respectively (see experimental section for synthesis protocol). Subsequently, X-ray diffraction (XRD), high resolution transmission electron microscopy (HRTEM) and inductively coupled plasma mass spectrometry (ICP-MS) were used to validate our structural design strategy. For all the catalysts, the XRD patterns displayed the typical LDHs facets (003), (006), (009), (110) and (113), even though the Ti containing samples showed poorer degree of crystallization **(**Fig. 1**A-B)** [28]. $TiO_x$ was not observed in the XRD diffractograms, however a positive shift in the peak positions of the (110) and (113) facets was noticed when Ti was incorporated into the catalysts, which suggested the successful introduction of Ti into the LDHs structure[36]. Furthermore, the ICP results confirmed the expected amount of Ti for each material **(**Table S1**)**. Besides, HRTEM images and AC-HAADF-STEM line scanning and mapping results **(**Fig. 1 **$C_1$-$C_8$ and** Figs. S1-S2**)** delineated the formation of an amorphous $TiO_x$ layer at the edges of the Ru nanoparticles (NPs), confirming the migration of Ti from the bulk to the surface through thermal reduction under $H_2/N_2$ atmosphere. Meanwhile, the Ru loading on all the catalysts was consistent with the expected amounts (Table S1), *i.e.,* 2.57 ± 0.02. The NPs' size distribution was quite similar for all the catalysts with 5.21 ± 0.95 nm, 5.07 ± 0.82 nm, 4.77 ± 0.70 nm and 4.95 ± 0.90 nm for $Ru/Mg_9Al_6O_x$, $Ru@TiO_x/Mg_9Al_6Ti_3O_x$, $Ru@TiO_x/Mg_9Al_6Ti_6O_x$ and $Ru@TiO_x/Mg_9Al_6Ti_9O_x$, respectively **(**Fig. S3**)**. For all the catalysts, the Ru NPs displayed a lattice spacing of *ca.* 0.224 nm, corresponding to the Ru (111) facet **(**Fig. S1**)**[37].

Subsequently the influence of the $TiO_x$ layer on the Ru coordination

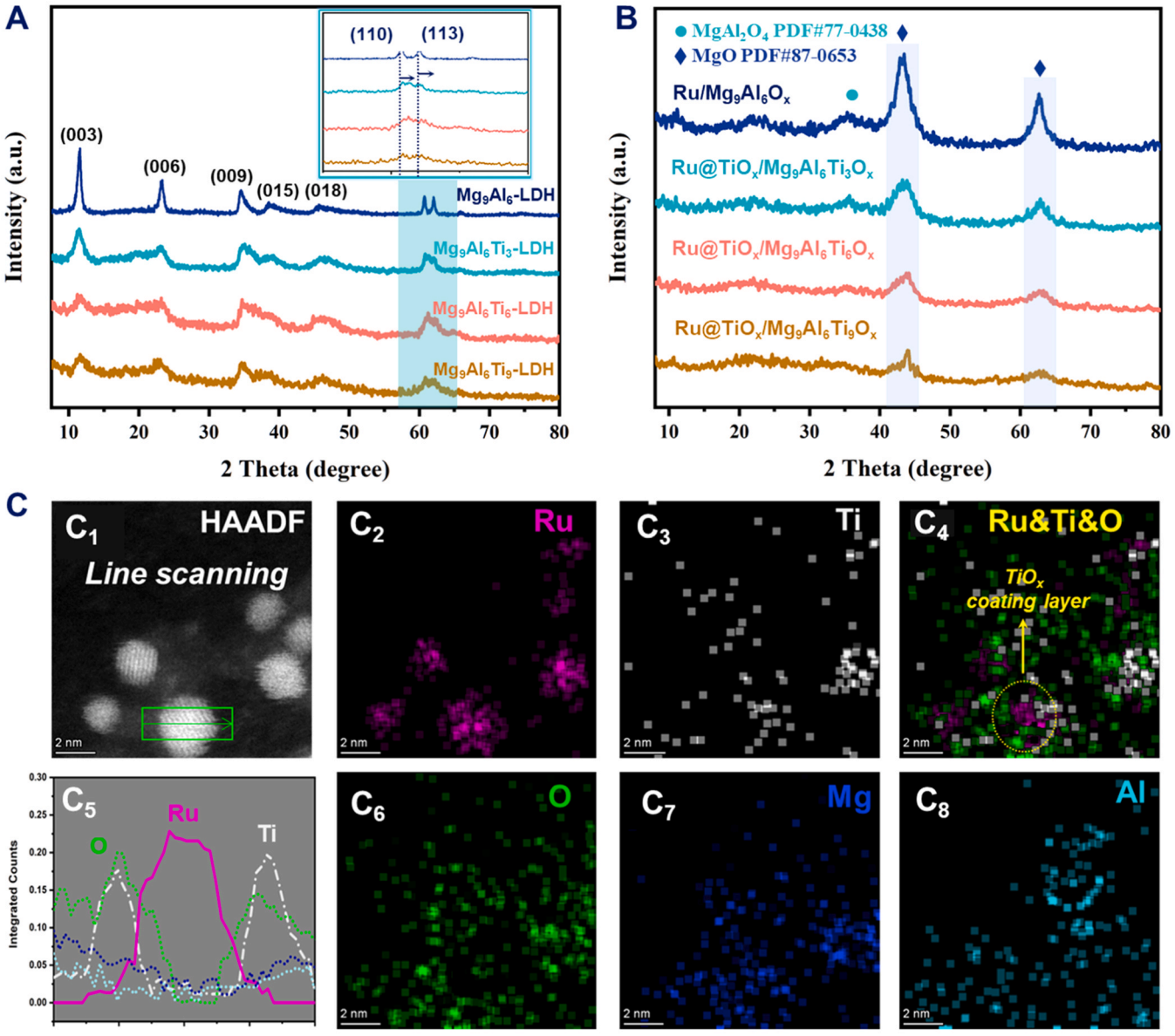


**Fig. 1.** (A) XRD patterns of $Mg_9Al_6$-LDHs, $Mg_9Al_6Ti_3$-LDHs, $Mg_9Al_6Ti_6$-LDHs and $Mg_9Al_6Ti_9$-LDHs (B) XRD patterns of $Ru/Mg_9Al_6O_x$, $Ru@TiO_x/Mg_9Al_6Ti_3O_x$, $Ru@TiO_x/Mg_9Al_6Ti_6O_x$ and $Ru@TiO_x/Mg_9Al_6Ti_9O_x$. (C) AC-HAADF-STEM images as well as line scanning and mapping results for $Ru@TiO_x/Mg_9Al_6Ti_6O_x$.

number was investigated by carrying CO chemisorption experiments (Table S1 **and** Fig. S4**)**. The Ru NPs dispersion calculation from CO-pulse experiments was compared with HRTEM statistics and revealed significant differences between both techniques for all the catalysts, except for $Ru/Mg_9Al_6O_x$. More specifically, the results from the CO-pulse experiments were lower for $Ru@TiO_x/Mg_9Al_6Ti_3O_x$, $Ru@TiO_x/Mg_9Al_6Ti_6O_x$ and $Ru@TiO_x/Mg_9Al_6Ti_9O_x$, compared to the results from HRTEM. This is due to the partial coverage of the metal NPs by metal oxides, which often results in the reduction/suppression of CO adsorption on the metal NPs and often leads to erroneous measurement. To further investigate the influence of the oxide layer on Ru, *in situ* DRIFT experiments were performed under CO atmosphere [13,38]. The ratio of linear-CO bond to bridged-CO bond areas on Ru, increased from 0.79 for $Ru/Mg_9Al_6O_x$ to 0.97, 1.09 and 1.14 for $Ru@TiO_x/Mg_9Al_6Ti_3O_x$, $Ru@TiO_x/Mg_9Al_6Ti_6O_x$ and $Ru@TiO_x/Mg_9Al_6Ti_9O_x$, respectively **(**Fig. 2**A)**. The difference between the CO adsorption modes arises from the coordination environment of Ru. Indeed, CO tends to adopt a linear adsorption mode when bound to Ru-O sites, while it exhibits a bridged adsorption mode on Ru-Ru sites [13]. Our preliminary hypothesis was to consider that the $TiO_x$ coating layer might alter the coordination structure of Ru NPs. In the aim to validate this, we performed Extended X-ray adsorption fine structure (EXAFS) analyses on the catalysts. The results delineated, for all the catalysts, the presence of two coordination states of Ru, *viz.* Ru-O path centered at around 1.97 Å and metallic Ru-Ru path centered at around 2.67 Å [39–41]. In the absence of Ti, the Ru-O to Ru-Ru ratio was 1.02.

As the amount of Ti increases this ratio rose to 1.18, 1.21 and 1.26 for $Ru@TiO_x/Mg_9Al_6Ti_3O_x$, $Ru@TiO_x/Mg_9Al_6Ti_6O_x$ and $Ru@TiO_x/Mg_9Al_6Ti_9O_x$ respectively, demonstrating a linear relationship between Ti amount and Ru-O to Ru-Ru ratio **(**Fig. 2**B-E,** Table S2 **and** Fig. S5**)**. The results substantiate the crucial role of $TiO_x$ in regulating the coordination structure of Ru.

X-ray absorption near edge structure (XANES) was subsequently conducted to investigate the effect of the coordination structure on the chemical environment and electronic structure of the catalysts (Fig. S6**)**. The results show that Ru remains in its metallic state when coordinated with another Ru atom (Ru-Ru), but its oxidation state increases ($Ru^{\delta+}$) when coordinated with an O atom (Ru-O), due to the higher

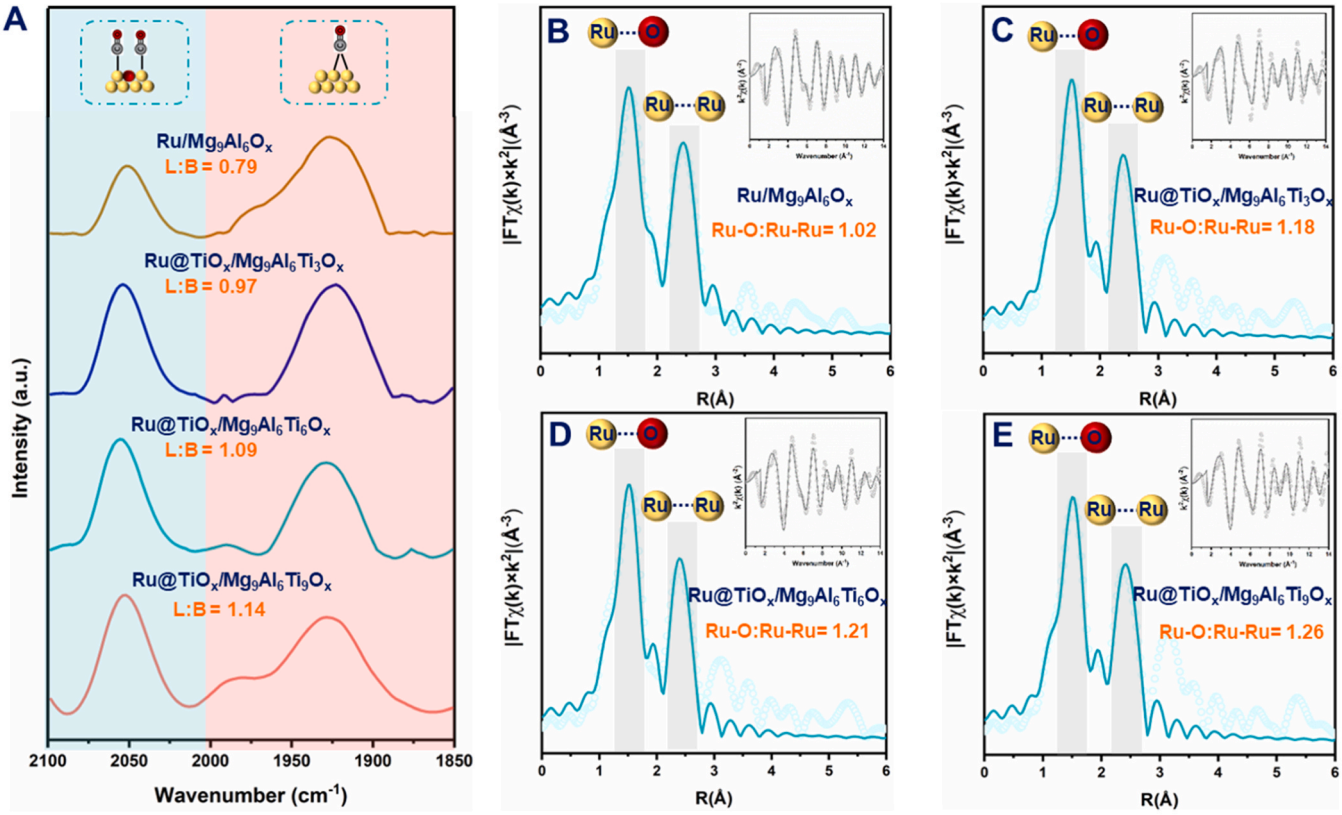


**Fig. 2.** (A) CO *in situ* DRIFT spectra and (B-E) Fourier transformed EXAFS spectra with $k^2$-weighted magnitude at Ru K-edge of series catalysts (without phase correction) the illustration is $k^2$-weighted χ(k) data for $Ru/Mg_9Al_6O_x$, $Ru@TiO_x/Mg_9Al_6Ti_3O_x$, $Ru@TiO_x/Mg_9Al_6Ti_6O_x$ and $Ru@TiO_x/Mg_9Al_6Ti_9O_x$.

electronegativity of O (3.44) compared to Ru (2.20). This, is further confirmed by X-ray photoelectron spectroscopy (XPS), which display a peak area ratio of $Ru^{\delta+}/Ru^0$ of 0.89 in $Ru/Mg_9Al_6O_x$, that increases to 1.20 in $Ru@TiO_x/Mg_9Al_6Ti_9O_x$. Moreover, The XPS data revealed a negative shift of the binding energy of $Ru^0$ species for the catalysts containing Ti. This shift was accompanied with a positive shift of the binding energy of $Ti^{4+}$, *ca.* 0.3 eV (Fig. S7), denoting an electron donating effect of Ti. This also suggests the presence of a strong metal support interaction (SMSI) within those catalysts. The data collectively, confirmed that our synthesis method led to the successful decoration of Ru NPs by $TiO_x$ layer, that not only directly creates more asymmetric Ru-O coordination structure but also SMSI, with electron-enriched Ru sites (Fig. 3).

### 3.2. Catalytic performances

After clarifying the physicochemical properties and micro-regional structures of the catalysts, the catalytic performances were evaluated in a stainless-steel autoclave at 180 °C under 0.55 MPa $NH_3$ and 0.4 MPa $H_2$ and the results are displayed in Fig. 4**A-D**. $Ru/Mg_9Al_6O_x$ exhibits the highest 1-octanol conversion, achieving 93 % in only 6 h and reaching 100 % within 24 h. However, its 1-octylamine selectivity was the lowest among the catalysts, reaching only 61.0 % ± 2.6 % after 9 h. Although, the imine couldn't be detected by gas chromatography, its presence in the reaction system can be inferred from the 1-octylamine selectivity against octanol conversion. Indeed, the coexistence of 1-octylamine and a large amount of imine leads to dimerization reactions. The presumed high concentration of imine, could likely explained the formation of the dioctylamine that reaches a selectivity of 15.0 %. After 9 h reaction, the 1-octylamine selectivity dropped down from 61.3 % to only 32.0 % and was accompanied with a further increase of the dioctylamine selectivity to 25.3 %. The catalysts, with Ti content, demonstrated a distinct behavior with a lower 1-octanol conversion and a higher selectivity to octylamine. Furthermore, we conducted the catalytic performance testing on a Ru/MgO sample under identical reaction conditions to those used for $Ru@TiO_x/Mg_9Al_6Ti_6O_x$ shown (Fig. S8). After 36 h of reaction, complete conversion of 1-octanol was achieved within 24 h. The yield of 1-octylamine reached a maximum of 71.7 ± 2.1 % at 12 h but gradually

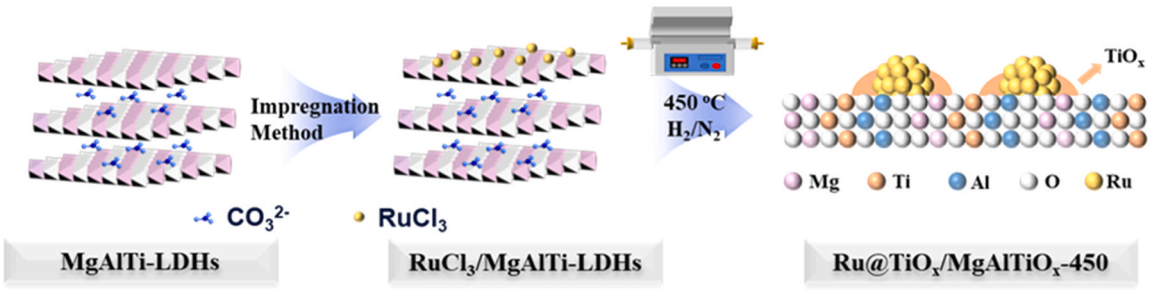


**Fig. 3.** Catalyst formation process taking $Ru@TiO_x/Mg_9Al_6Ti_6O_x$ as an example.

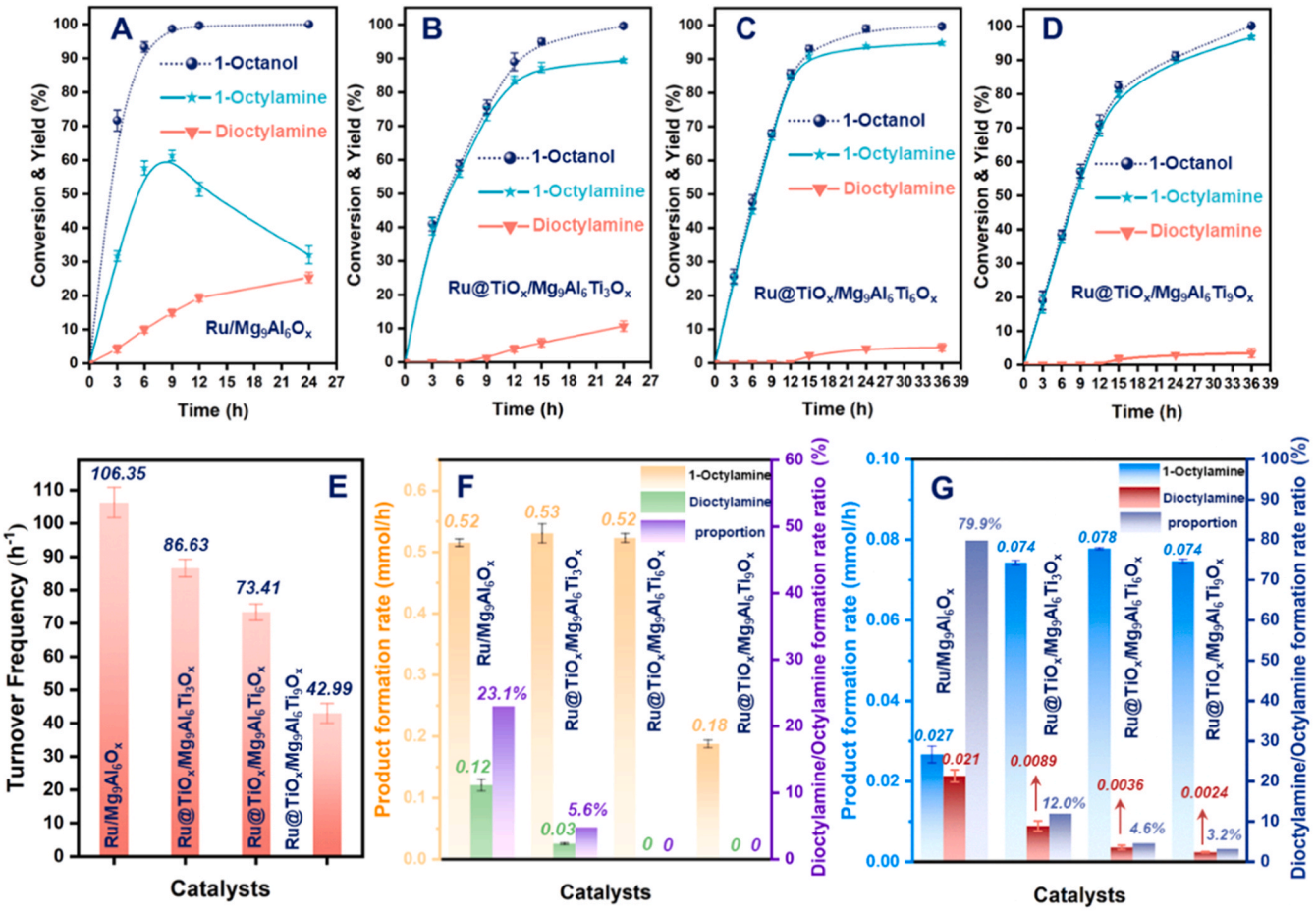


**Fig. 4.** (A-D) 1-octanol conversion, 1-octylamine and dioctylamine yield within the time course of the reaction, for the catalyst series, (E) TOF value (F) products formation rate and dioctylamine to 1-octylamine ratio, within the kinetic range of 1.5 h, (G) products formation rate and dioctylamine to 1-octylamine ratio within 24 h.

declined to 57.3 ± 2.1 % during the 12–36 h reaction period. This decline was accompanied by a further increase in dioctylamine yield to 24.7 ± 1.5 %. The product yield versus time for Ru/MgO was similar to that of $Ru/Mg_9Al_6O_x$. The formation of dioctylamine can be attributed to dimerization reactions between 1-octylamine and the imine, as well as the imine self-dimerization (see Scheme 1). Throughout the reaction monitoring, we observed a continuous increase in dioctylamine yield. Additionally, 1-octylamine yield initially increased to 71.7 ± 2.1 % but subsequently decreased to 57.3 ± 2.1 %. These results suggest that the Ru/MgO catalyst has limitations in rapidly converting the imine to 1-octylamine, thus promoting the by-product formation through dimerization reactions. This, further highlights the superior role of the $Ru@TiO_x/Mg_9Al_6Ti_6O_x$ catalyst in promoting the rapid imine conversion.

Subsequently the intrinsic activity was assessed. As shown in Fig. 4**E**, overall, the catalysts demonstrated an intrinsic activity (TOF value, calculated using **Supporting Formula 1**) sequence of $Ru/Mg_9Al_6O_x$ (106.35 $h^{-1}$) > $Ru@TiO_x/Mg_9Al_6Ti_3O_x$ (86.63 $h^{-1}$) > $Ru@TiO_x/Mg_9Al_6Ti_6O_x$ (73.41 $h^{-1}$) > $Ru@TiO_x/Mg_9Al_6Ti_9O_x$ (42.99 $h^{-1}$), which was consistent with the conversion *vs.* time. For $Ru/Mg_9Al_6O_x$, the conversion reached 100 % within 9 h, while for $Ru@TiO_x/Mg_9Al_6Ti_3O_x$, $Ru@TiO_x/Mg_9Al_6Ti_6O_x$, $Ru@TiO_x/Mg_9Al_6Ti_9O_x$ the time was prolonged to 24 h and 36 h, respectively. However, their selectivity to 1-octylamine displayed an inverse relationship with the sequence: $Ru/Mg_9Al_6O_x$ (32.0 %) < $Ru@TiO_x/Mg_9Al_6Ti_3O_x$ (89.3 %) < $Ru@TiO_x/Mg_9Al_6Ti_6O_x$ (94.6 %) < $Ru@TiO_x/Mg_9Al_6Ti_9O_x$ (96.7 %). Those results indicate that the presence of Ti in the catalysts reduces the dimerization pathway and enhances the selectivity toward 1-octylamine. Furthermore, the product formation rates were measured at 1.5 h in the kinetic range and at 24 h when the reaction was almost complete (Fig. 4 **F**). From the data, the total production formation rate displays the following sequence $Ru/Mg_9Al_6O_x$ (0.64 mmol/h) > $Ru@TiO_x/Mg_9Al_6Ti_3O_x$ (0.56 mmol/h) > $Ru@TiO_x/Mg_9Al_6Ti_6O_x$ (0.52 mmol/h) > $Ru@TiO_x/Mg_9Al_6Ti_9O_x$ (0.18 mmol/h), reflecting the order of catalysts activity, which was consistent with the aforementioned results. It should be noted that over $Ru/Mg_9Al_6O_x$, the formation rate of the dioctylamine (0.12 mmol/h) accounted for 23.1 % of the total formation rate. This ratio dropped down dramatically as the Ti is increased within the catalyst, *viz.* over $Ru@TiO_x/Mg_9Al_6Ti_3O_x$, the dioctylamine formation rate was only 0.03 mmol/h, accounting for 5.6 % of the total formation rate, while over $Ru@TiO_x/Mg_9Al_6Ti_6O_x$ and $Ru@TiO_x/Mg_9Al_6Ti_9O_x$, the figure was zero. After 24 h of reaction, the behavior of the catalysts changed drastically (Fig. 4 **G**). The 1-octylamine production rate for the Ti-free catalyst was only 0.027 mmol $h^{-1}$, whereas the Ti-containing catalysts exhibited significantly higher rates of 0.074, 0.078, and 0.074 mmol $h^{-1}$, for $Ru@TiO_x/Mg_9Al_6Ti_3O_x$ $Ru@TiO_x/Mg_9Al_6Ti_6O_x$ $Ru@TiO_x/Mg_9Al_6Ti_9O_x$ respectively, *ca.* three times higher. Among them, $Ru@TiO_x/Mg_9Al_6Ti_6O_x$ showed the highest activity. Meanwhile, the production rate of dioctylamine decreased from 0.021 to 0.0024 mmol/h with the augmentation of Ti content within the catalysts, proving that Ti content plays an important role in preventing the formation of the by-product dioctylamine.

The standard reaction conditions used were 0.55 MPa $NH_3$ and 0.4 MPa $H_2$. We then investigated the effect of $NH_3$ by varying its

pressure to 0.1 MPa, 0.2 MPa, and 0.3 MPa, while keeping the $H_2$ pressure constant at 0.4 MPa. The resulting catalytic performance of the $Ru@TiO_x/Mg_9Al_6Ti_6O_x$ catalyst showed a clear dependence on $NH_3$ pressure. Indeed, as the $NH_3$ pressure increased from 0.1 MPa to 0.2 MPa and then to 0.3 MPa, the 1-octanol conversion after 36 h rose from 54 % to 77 %, and ultimately reached 100 %. $NH_3$ plays a crucial role in the amination process, *viz.* insufficient $NH_3$ pressure hinders the conversion of octanal to the imine, leading to lower catalytic activity (Fig. S9). In the next stage, we fixed the $NH_3$ pressure at 0.55 MPa and varied the $H_2$ pressure to 2 MPa, 1 MPa, 0.2 MPa, and 0.1 MPa, corresponding to $H_2/NH_3$ ratios of 3.64, 1.82, 0.36, and 0.18, respectively. The results showed that higher $H_2/NH_3$ ratios led to poorer catalytic performance. At ratios of 3.64 and 1.82, the 1-octanol conversion after 36 h was only 66 % and 47 %, respectively. Although lower $H_2/NH_3$ ratios (0.36 and 0.18) significantly improved the catalytic activity, achieving 100 % conversion within 12 h and 9 h, respectively, an undesired by-product, 1-octylnitrile, was also formed. As outlined in the reaction Schemes 1, 1-octylnitrile is generated through further dehydrogenation of 1-octylamine. Under $H_2/NH_3$ ratios of 0.36 and 0.18, the yields of 1-octylnitrile were 36 % and 41 %, respectively. These results suggest that an appropriate balanced $H_2/NH_3$ ratio is crucial to suppress excessive dehydrogenation of 1-octylamine and improve the selectivity toward the desired 1-octylamine product (Fig. S10).

The plot of the TOF values against the Ru-Ru bond percentage **(**Fig. 5 **A)** displayed a positive linear correlation, suggesting the important role of $Ru^0$ in the 1-octanol conversion. Furthermore, a positive linear relationship was observed between the Ru-O/Ru-Ru bond ratio and octylamine selectivity, while a negative one was identified with dioctylamine **(**Fig. 5**B-C)**. These results suggested that Ru-O bonds promote the hydrogenation process and avoid the imine accumulation. The effect of $H_2$ pressure was then evaluated against the TOF values (Fig. S11), at fixe $NH_3$ pressure (0.55 MPa). At 0.4 MPa $H_2$ pressure, the TOF value was 73.41 $h^{-1}$ and decreased to 55.26 $h^{-1}$, 47.13 $h^{-1}$, and 41.89 $h^{-1}$ when the $H_2$ pressure reached 1.4, 2.4, and 3.4 MPa, respectively. This trend suggests that elevated $H_2$ pressure negatively affects the catalytic activity.

Moving forward the best catalyst in term of conversion and 1-octylamine selectivity, *i.e.* $Ru@TiO_x/Mg_9Al_6Ti_6O_x$, was selected to evaluate its stability for four cycles against $Ru/Mg_9Al_6O_x$ (see experimental section for protocol). As shown in Fig. 5**D**, the $Ru@TiO_x/Mg_9Al_6Ti_6O_x$ catalyst can be reused for four cycles without any noticeable decline in 1-octylamine yield. However, in the 5th run, both the 1-octanol conversion and 1-octylamine yield slightly decreased from 33 % to 28 % and from 32 % to 27 %, respectively. We also conducted BET and HRTEM to investigate the factors leading to the catalyst deactivation. For the fresh $Ru@TiO_x/Mg_9Al_6Ti_6O_x$ catalyst, the BET surface area was *ca.* 111 $m^2/g$, with a pore volume of 0.38 $cm^3/g$ and an average pore size of *ca.*12 nm. In contrast, the used catalyst exhibited a markedly reduced surface area of *ca.* 53 $m^2/g$, a pore volume of 0.14 $cm^3/g$, and a slight smaller pore size of *ca.* 10 nm (Fig. S12 **and** Table S3). Moreover, The TEM images reveal a slight increase of the particle size from 4.77 ± 0.70 nm of fresh $Ru@TiO_x/Mg_9Al_6Ti_6O_x$ catalyst to 5.53 ± 0.99 nm of used $Ru@TiO_x/Mg_9Al_6Ti_6O_x$ catalyst (Fig. S13). Based on these post-reaction characterizations, we conclude that the main factors affecting the catalyst activity is the decrease in the surface area. Meanwhile, the catalyst without Ti exhibited a rapid decline in activity of 64 % (Fig. 5**E**). Our best catalyst was benchmarked against the state-of-the-art catalysts based on several key metrics *i.e.,* TOF, 1-octylamine yield, reusability and $NH_3$ pressure. In terms of activity, the TOF value of $Ru@TiO_x/Mg_9Al_6Ti_6O_x$ demonstrated a 1.1–29.1 folds improvement compared to current catalysts. Regarding the 1-octylamine yield, the catalyst also exhibited a promotion effect of 11.0–32.2 %. Notably, this catalyst overcame the long-standing challenge of reusability, maintaining stability over four consecutive cycles. Furthermore, $Ru@TiO_x/Mg_9Al_6Ti_6O_x$ operates under milder reaction conditions (*i.e.* 0.55 MPa vs. 0.4–1.4 MPa) compared to the state-of-the-art, with $NH_3$ pressure being

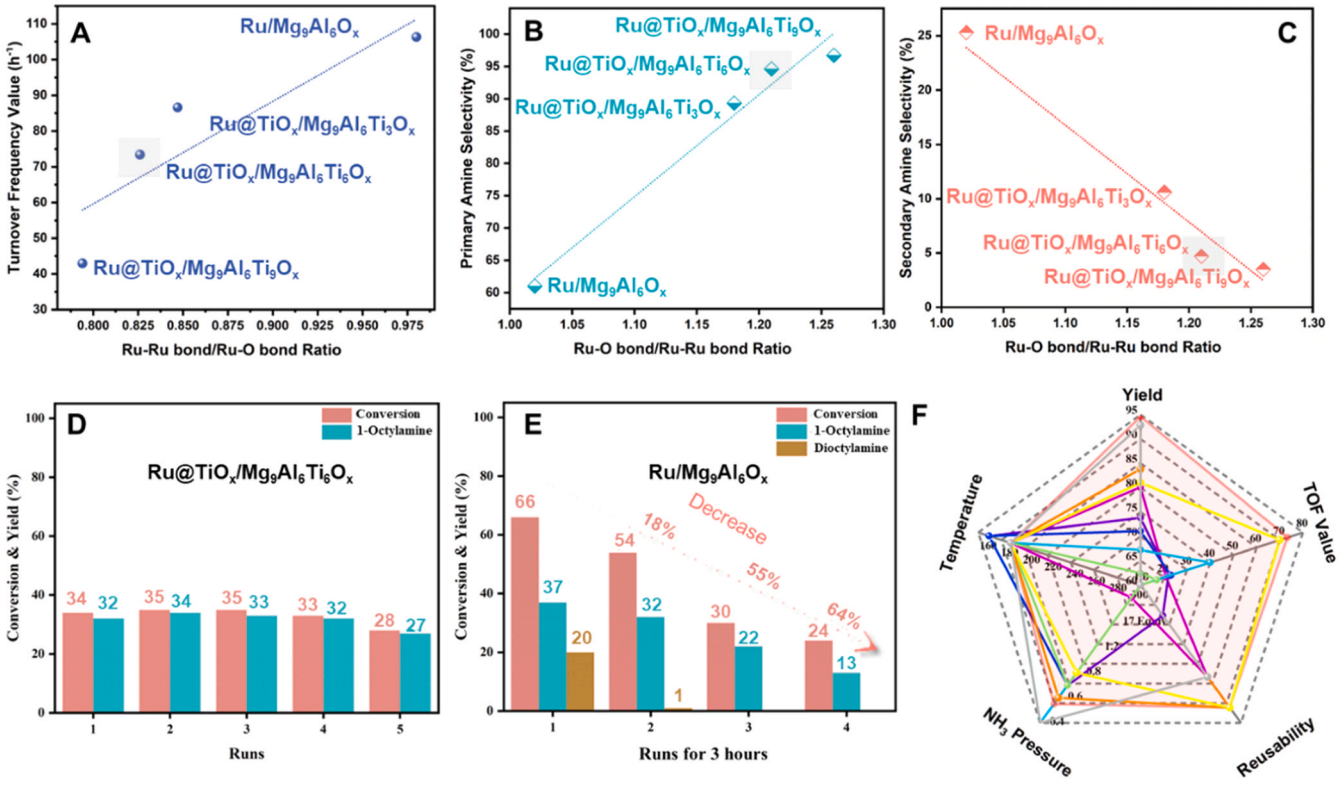


**Fig. 5.** (A) Relationship between Ru-Ru bond ratio and TOF value (B) relationship between Ru-O/Ru-Ru bond ratio with primary amine selectivity; (C) relationship between Ru-O/Ru-Ru bond ratio with secondary amine selectivity, (D-E) catalyst reusability test results, (F) radar chart for catalytic performance comparison.

among the lowest (Table S4). Moreover, our catalyst achieved the highest TOF value of 73.4 $h^{-1}$ and a 1-octylamine yield of 94.6 %, surpassing all reported references, despite having a relatively low Ru loading of just 2.56 wt. %. These features position our catalyst among the most advanced reported to date (Fig. 5 **F** and Table S4) [19,20,42–47].

The possibility of leaching, and thus the potential involvement of homogeneous Ru catalysis, was ruled out by performing hot filtration and ICP analysis of the post-reaction solution (Fig. S14). To further confirm the absence of leaching, C(XC72R) was utilized as adsorbent to capture potential Ru ions in the reaction solution[48]. After the reaction, the catalyst was separated, and C was introduced into the hot reaction solution and stirred for 1 h. The C was then collected from the reaction mixture, and HRTEM was employed to examine any Ru adsorbed on its surface. The data indicated that no Ru was present on the C. Therefore, the catalyst demonstrated very good stability against leaching, making it suitable for practical application (Fig. S15-S16 **and** Table S5**)**.

Subsequently, we have explored the substrate scope of the catalyst by employing a range of seven different aldehydes and eight different alcohols (Fig. S17). The catalyst exhibited consistent performance across this diverse set of substrates, demonstrating its broad applicability.

### 3.3. *Structure-performance relationship and catalytic mechanism investigation*

*In situ* Fourier-transform infrared spectroscopy (FTIR) coupled with isotopic experiments (see experimental section for protocol) was conducted to gain insight into the mechanism. Over $Ru@TiO_x/Mg_9Al_6Ti_6O_x$ and upon activation by $H_2$, a broad band between 3550 and 3300 $cm^{-1}$ is observed and attributed to OH groups, indicating the interaction of hydrogen with oxygen atoms[24,49]. Additionally, a relatively weak IR band at 1958 $cm^{-1}$ was observed and attributed to Ru-H species. The data suggest a heterolytic cleave of $H_2$ over the catalyst. This finding is further supported by the H-D isotope labeling experiments, where IR bands of O-D were observed at 2624, 2486, and 2458 $cm^{-1}$. The calculated $\nu_{O\text{-}H}/\nu_{O\text{-}D}$ ratio of 1.36 (Fig. 6 **A),** aligns well with the expected isotope shift, confirming that protons (or deuterons) are bonded to oxygen atoms[24,49]. Over $Ru/Mg_9Al_6O_x$, although $O\text{-}H^+$ and $Ru\text{-}H^-$ bands are still observed in the IR spectra, the $Ru\text{-}H^-$ band is significantly weaker compared to that of $Ru@TiO_x/Mg_9Al_6Ti_6O_x$. This suggests that, in the $Ru/Mg_9Al_6O_x$ sample, only a negligible fraction of $H_2$ undergoes heterolytic cleavage (Fig. 6**B**)[24,49]. We further synthesized a Ru/MgO sample to investigate the $H_2$ activation mechanism proposed in this study. FT-IR analysis was performed, and the results revealed a weak $Ru\text{-}H^-$ stretching band at 1962 $cm^{-1}$, along with a strong $O\text{-}H^+$ band observed in the range of 3355–3488 $cm^{-1}$(Fig. S18**)**. Similar to the spectra obtained for $Ru/Mg_9Al_6O_x$, this indicates that only a small portion of $H_2$ underwent heterolytic cleavage on the Ru/MgO surface, while the majority of the $H_2$ was activated *via* homolytic cleavage. The above results indicated that $H_2$ undergoes heterolytic dissociation, induced by $Ru^{\delta+}$ and the surrounding oxygen atoms in $Ru@TiO_x/Mg_9Al_6Ti_6O_x$, generating $O\text{-}H^+$ and $Ru\text{-}H^-$ species.

To further investigate the catalytic role of $Ru\text{-}H^-$ and $O\text{-}H^+$ species, N-Benzylidenebenzylamine with an identical C═N group as imine, was selected as a probe molecule to investigate the hydrogenation process on $Ru@TiO_x/Mg_9Al_6Ti_6O_x$, as the imine intermediate is not commercially available. The resulting reaction order with respect to $H_2$ is 0.895 (Fig. 7 **A)**, suggesting that one hydrogen species plays an important role in the rate-determining step[24]. In order to identify the specific hydrogen species involved, the kinetic isotope effect (KIE) was examined using $H_2$ and $D_2$ as probe molecules under kinetic control. The resulting KIE ($k_H/k_D$) is 2.58 (Fig. 7**B)**[24,50]. The theoretical calculations (**Supporting Formula 2**) indicated that if an electrophilic attack on the C═N bond occurs *via* the $H^+$ species, the predicted $k_H/k_D$ value would be 4.30. If instead it is through a nucleophilic attack, *via* $H^-$ species, the expected $k_H/k_D$ value would be 2.40, which aligns more with the obtained KIE. Moreover, we also conducted the hydrogenation experiment over $Ru/Mg_9Al_6O_x$ catalyst, and the calculated slope was 1.853. Different from the hydrogenation process on $Ru@TiO_x/Mg_9Al_6Ti_6O_x$, this phenomenon suggested that two hydrogen species are involved in the rate-determining step. This implies that $H_2$ likely undergoes homolytic cleavage into two H* atoms, which then participate in the hydrogenation of the imine intermediate (Fig. 7 **C)**. We conducted a kinetic isotope effect (KIE) experiment over the $Ru/Mg_9Al_6O_x$ catalyst, which gave a value of 3.98, indicating that O-H species play a significant role in the hydrogenation process (Fig. 7**D)**. Since $Ru/Mg_9Al_6O_x$ facilitates only a small fraction of heterolytic $H_2$ cleavage while most $H_2$ undergoes homolytic cleavage, and considering that the Ru-H bond is relatively weak, it is reasonable to speculate that the produced H* species spill over to oxygen atoms, forming a distinct O-H peak. This observation aligns with our above FT-IR results and $H_2$-TPD data (Fig. 6 **and** Fig. S19**)**.

Additionally, Density Functional Theory (DFT) calculations were performed to provide critical insights into the hydrogenation process of

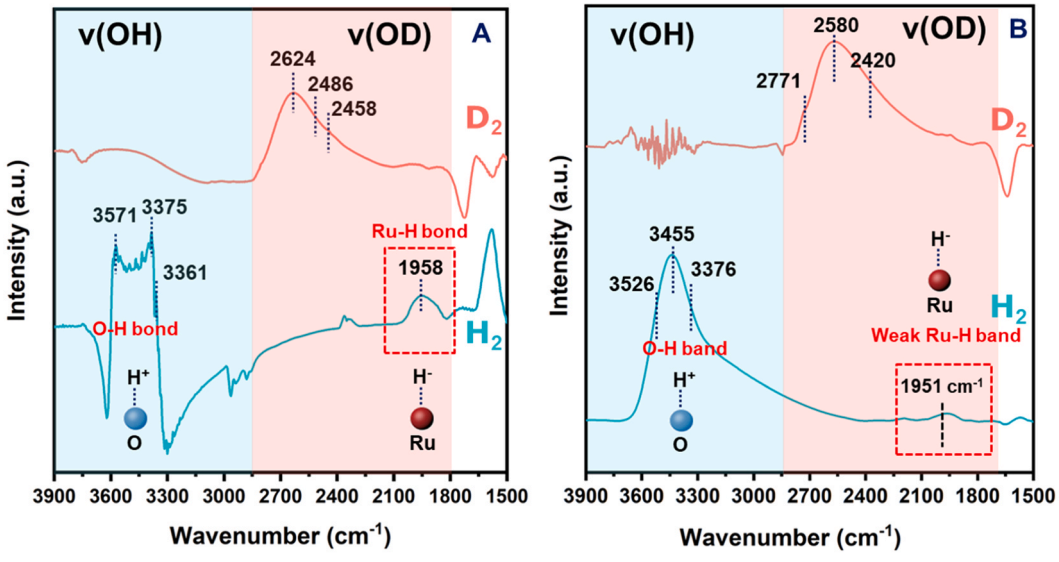


**Fig. 6.** (A) H-D *in situ* FT-IR experiment over $Ru@TiO_x/Mg_9Al_6Ti_6O_x$; (B) H-D *in situ* FT-IR experiment over $Ru/Mg_9Al_6O_x$.

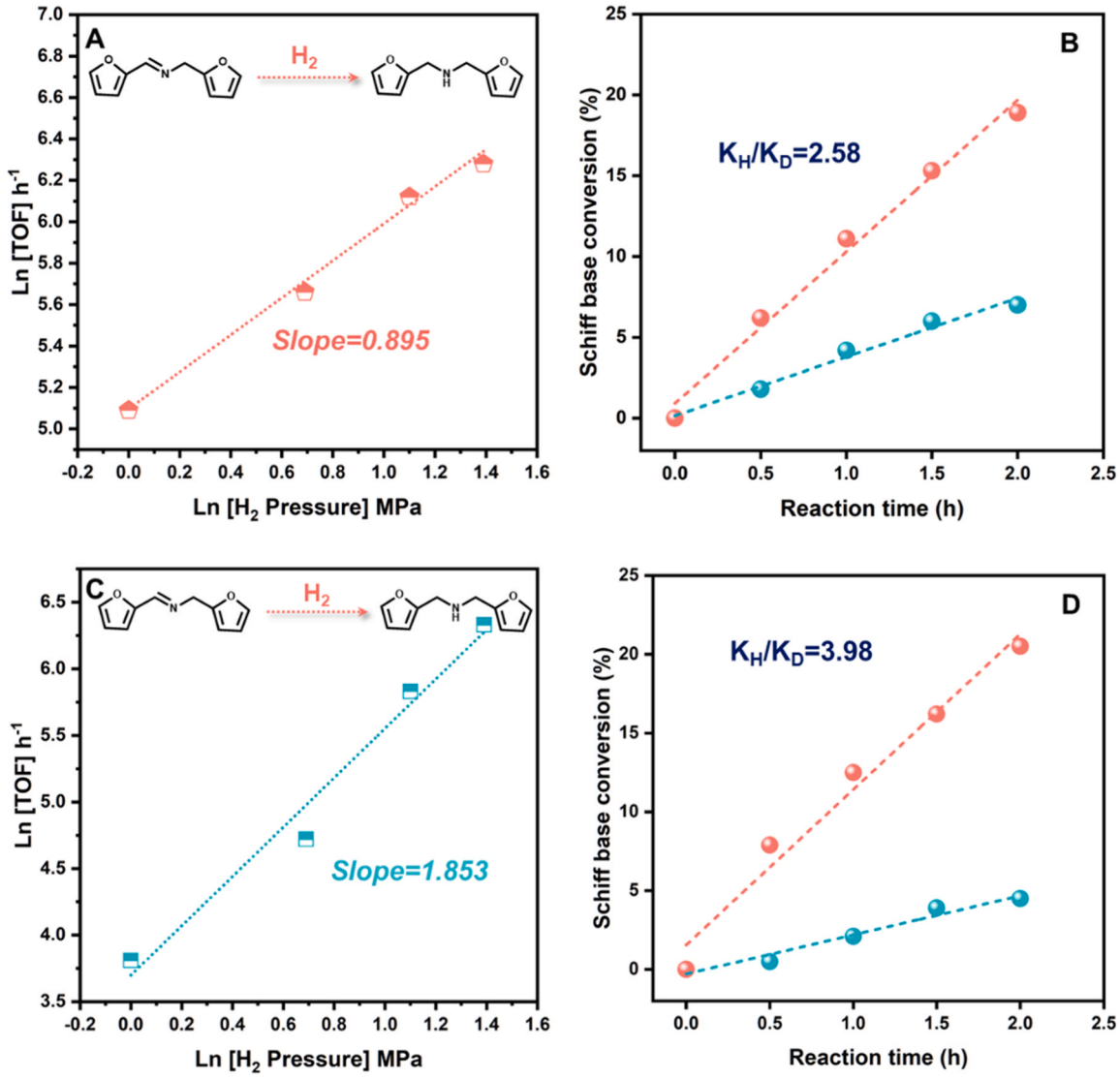


**Fig. 7.** (A) $H_2$ pressure dependence during the hydrogenation process over Ru@TiOx/$Mg_9Al_6Ti_6O_x$, (B) KIE experiment over Ru@TiOx/$Mg_9Al_6Ti_6O_x$, (C) $H_2$ pressure dependence during the hydrogenation process over Ru/$Mg_9Al_6O_x$ and (D) KIE experiment over Ru/$Mg_9Al_6O_x$.

imine. Both heterolytic and homolytic dissociation pathways of $H_2$ and the hydrogenation process were examined. The homolytic dissociation, producing two $H^{\cdot}$ radicals, showed an energy barrier of 0.81 eV for the initial attack on the $C^{\delta+}$ site in the C═N group, and 0.095 eV for the subsequent attack on the $N^{\delta-}$ site, indicating an unfavorable pathway due to the high initial energy barrier (Fig. 8 **A**). In sharp contrast, the

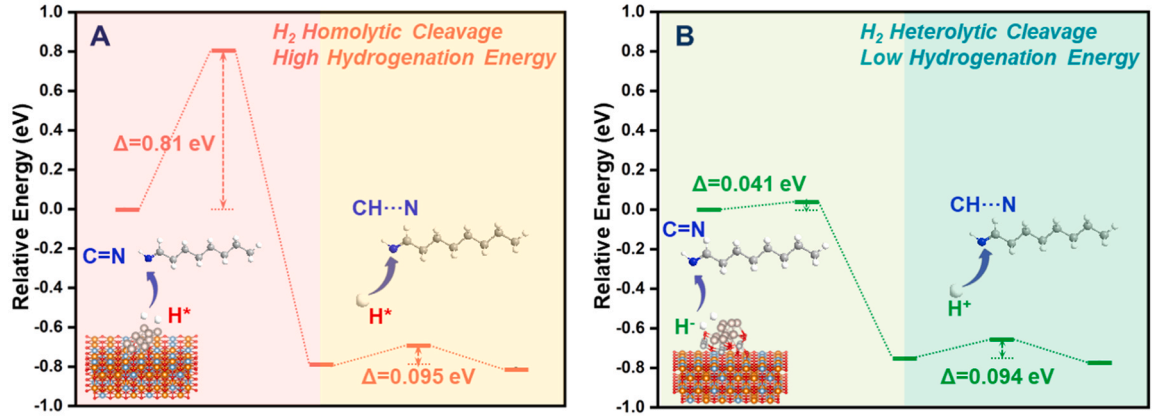


**Fig. 8.** (A) Barrier energy, on key steps, on homolytic cleavage of $H^{\cdot}$ attack on C═N group; (B) Barrier energy, on key steps, on heterolytic cleavage of $H^{-}$ and $H^{+}$ attack on C═N group. Gray ball on top: Ru atom; orange ball: Mg atom; blue ball: Al atom, red ball: O atom and ashen ball surrounding to the gray ball: Ti atom.

heterolytic dissociation, yielding $H^-$ and $H^+$ active species, demonstrated a significantly lower energy barriers *viz.* only 0.041 eV for $H^-$ attacking the $C^{\delta+}$ sites and only 0.094 eV for $H^+$ attacking the $N^{\delta-}$ sites **(**Fig. 8**B)**. The data highlight the heterolytic dissociation of $H_2$ as the key step for efficient hydrogenation, facilitating the rapid conversion of imine to octylamine and preventing dimerization by-products formation. This mechanistic understanding emphasizes the superior catalytic function of $Ru@TiO_x/Mg_9Al_6Ti_6O_x$, driven by the Ru-$H^-$ and O-$H^+$ active species.

The $NH_3$-TPD results reveal that titanium incorporation significantly enhances the surface acidity (Fig. S20A). Indeed, the Ti-containing catalysts exhibit $NH_3$ desorption capacities ranging from 4.35 to 5.16 mmol $g^{-1}$, representing a notable increase compared to the 3.78 mmol $g^{-1}$ observed for the $Ru/Mg_9Al_6O_x$ catalyst. According to our previous studies and literature reports, enhanced acidity promotes activation of the C═N bond in *in situ* generated imines *via* interaction between the acidic sites and the nitrogen atom, thereby facilitating imine hydrogenation [13,15,51]. Similarly, the $CO_2$-TPD profiles demonstrate a substantial enhancement in basic sites availability upon Ti incorporation (Fig. S20B). The Ti-containing catalysts show $CO_2$ desorption capacities of 2.70–2.98 mmol $g^{-1}$, nearly doubling the basic sites density compared to the Ti-free catalyst (1.58 mmol/g). This significant increase indicates that titanium incorporation not only preserves the inherent basicity of the Mg-Al mixed oxide support but also introduces additional basic sites. This increased basicity plays a critical role in modulating the electronic structure of the supported Ru nanoparticles. Surface basic sites, such as lattice oxygen or hydroxyl groups, are known to interact strongly with metal species, donating electron density and strengthening metal–support interactions. In this context, the stronger interaction between Ru and the more basic Ti-modified supports likely leads to a higher electron density on Ru compared to the less basic $Ru/Mg_9Al_6O_x$ catalyst. This increase in electron density is particularly important for facilitating the heterolytic cleavage of $H_2$. Indeed, prior studies have demonstrated that electron-rich Ru sites possess enhanced $H_2$ activation capabilities, which can directly influence both the rate and efficiency of hydrogenation reactions [51]. Therefore, the observed enhancements in both acidity and basicity in the Ti-containing catalysts work synergistically to improve the overall catalytic performance.

Based on the data collected so far, the following mechanism (Scheme 2) can be proposed: (1) first, the dehydrogenation of 1-octanol to octanal occurs *via* the adsorption of the -OH group of 1-octanol on adjacent Ru-Ru sites, (2) the resulting octanal undergoes an amination process forming an imine intermediate, (3) the $H_2$ adsorbs on the Ru-O sites and undergoes a heterolytic cleavage leading to Ru-$H^-$ and O-$H^+$ species, (4) the $H^-$ species operates then a nucleophilic attack on the $C^{\delta+}$ sites of the C═N group of the imine. Simultaneously, the $H^+$ species operates an electrophilic attack on the $N^{\delta-}$ site of the C═N group of the imine, thereby rapidly completing the hydrogenation process to octylamine.

## 4. Conclusion

In this work, we have developed an effective strategy for addressing hydrogenation-mediated alcohol amination reactions, by precisely regulating the asymmetrical coordination environment of the catalyst's active sites. Ru-Ru and Ru-O sites were identified as critical in the dehydrogenation of 1-octanol to octanal and the subsequent heterolytic cleavage of $H_2$ for hydrogenation to octylamine. Using several advanced techniques such as EXAFS, *in situ* FTIR, H-D exchange FTIR, kinetic isotope experiments and DFT calculations, a mechanism was proposed. The C═N group in the imine intermediate undergoes a nucleophilic attack by $H^-$, followed by an electrophilic attack on the nitrogen atom by $H^+$, thereby completing the final hydrogenation process and ultimately yielding the desired product octylamine. This approach is particularly advantageous in scenarios where dehydrogenation and hydrogenation processes coexist. The high exogenous hydrogen pressure to drive hydrogenation process is not required, therefore dehydrogenation process

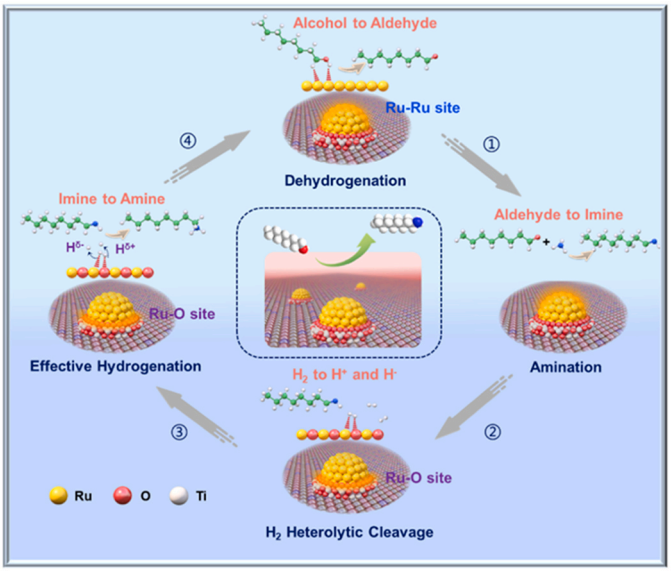


**Scheme 2.** Proposed catalytic mechanism of 1-octanol to octylamine over $Ru@TiO_x/Mg_9Al_6Ti_6O_x$.

was not impacted. Meanwhile, the hydrogenation of imine is promoted by induced $H^+/H^-$ with outstanding reactivity. The finely designed Ru-O value of 73.41 $h^{-1}$ under only 0.55 MPa $NH_3$ and 0.4 MPa $H_2$. Moreover, the stability of this catalyst over five cycles without any leaching, combined with a broad substrate applicability, positions it as a promising candidate for industrial applications. This work facilitates the development of more efficient and selective catalytic processes, enhancing the efficient utilization of hydrogen and ammonia resources. Additionally, it provides a framework for upgrading bulk chemical resources to high-value fine chemicals, thereby contributing to sustainable development.

## CRediT authorship contribution statement

**Zhexi Gao:** Writing – review & editing, Investigation. **Qian Wang:** Writing – review & editing, Investigation. **Haoran Ma:** Writing – review & editing, Investigation. **Huifang Wu:** Writing – review & editing, Investigation. **Richard Lewis:** Writing – review & editing, Supervision. **Dave Willock:** Writing – review & editing, Supervision, Investigation. **Ouardia Akdim:** Writing – review & editing, Writing – original draft, Supervision, Methodology, Formal analysis. **Junting Feng:** Writing – review & editing, Writing – original draft, Supervision, Funding acquisition. **Graham J. Hutchings:** Writing – review & editing, Supervision, Funding acquisition.

## Declaration of Competing Interest

The authors declare that they have no known competing financial interests or personal relationships that could have appeared to influence the work reported in this paper.

## Acknowledgements

This work was financially supported by the National Natural Science Foundation of China (22288102, 22208008), Fundamental Research Funds for the Central Universities (ZY2423), the Max Planck Centre for Fundamental Heterogeneous Catalysis (FUNCAT) and China Scholarship Council (CSC) program.

*Supporting Information*

Detailed information on catalysts characterizations and additional experiments (Figures S1-S20, Tables S1-S5 and Formulas 1–2).

## Appendix A. Supporting information

Supplementary data associated with this article can be found in the online version at doi:10.1016/j.apcatb.2025.125708.

## Data Availability

Data will be made available on request.

## References


[1] I. Delidovich, P.J.C. Hausoul, L. Deng, R. Pfützenreuter, M. Rose, R. Palkovits, Alternative monomers based on lignocellulose and their use for polymer production, Chem. Rev. 116 (2016) 1540–1599.

[2] A. Gandini, T.M. Lacerda, A.J.F. Carvalho, E. Trovatti, Progress of polymers from renewable resources: furans, vegetable oils, and polysaccharides, Chem. Rev. 116 (2016) 1637–1669.

[3] S. Bera, L.M. Kabadwal, D. Banerjee, Harnessing alcohols as sustainable reagents for late-stage functionalisation: synthesis of drugs and bio-inspired compounds, Chem. Soc. Rev. 53 (2024) 4607–4647.

[4] V. Froidevaux, C. Negrell, S. Caillol, J.-P. Pascault, B. Boutevin, Biobased amines: from synthesis to polymers; present and future, Chem. Rev. 116 (2016) 14181–14224.

[5] C. Fliedel, A. Ghisolfi, P. Braunstein, Functional short-bite ligands: synthesis, coordination chemistry, and applications of N-functionalized bis(diaryl/dialkylphosphino)amine-type ligands, Chem. Rev. 116 (2016) 9237–9304.

[6] Y. Park, Y. Kim, S. Chang, Transition metal-catalyzed C–H amination: scope, mechanism, and applications, Chem. Rev. 117 (2017) 9247–9301.

[7] Y. Liu, A. Afanasenko, S. Elangovan, Z. Sun, K. Barta, Primary benzylamines by efficient N-alkylation of benzyl alcohols using commercial Ni catalysts and easy-to-handle ammonia sources, ACS Sustain. Chem. Eng. 7 (2019) 11267–11274.

[8] Z. Xue, S. Wu, Y. Fu, L. Luo, M. Li, Z. Li, M. Shao, L. Zheng, M. Xu, H. Duan, Efficient light-driven reductive amination of furfural to furfurylamine over ruthenium-cluster catalyst, J. Energy Chem. 76 (2023) 239–248.

[9] X. Chen, S. Song, H. Li, G. Gözaydın, N. Yan, Expanding the boundary of biorefinery: organonitrogen chemicals from biomass, Acc. Chem. Res. 54 (2021) 1711–1722.

[10] n-Octylamine (CAS 111-86-4) Market Report | Global Forecast To 2028, ⟨https://industrygrowthinsights.com⟩.

[11] R. Coeck, J. Meeprasert, G. Li, T. Altantzis, S. Bals, E.A. Pidko, D.E. De Vos, Gold and silver-catalyzed reductive amination of aromatic carboxylic acids to benzylic amines, ACS Catal. 11 (2021) 7672–7684.

[12] R.W. Johnson, E. Fritz, Ind. Fat. Acids their Appl. (1992).

[13] Z. Gao, L. Cai, H. Ma, Y. Zhao, H. Wu, H. Liu, Q. Wang, D. Li, J. Feng, Dual scale hydrogen transfer bridge construction for biomass tandem reductive amination, ACS Catal. 13 (2023) 12835–12847.

[14] H. Wu, Q. Wang, Y. Zhao, Z. Gao, Y. Lin, L. Zheng, D. Li, J. Feng, Coupling cross-dimensional $Ru_1$–$Ru_n$ sites in confined nanoislands to overcome the limitation of coadsorption and diffusion in tandem reactions, ACS Catal. 14 (2024) 1584–1594.

[15] Z. Gao, X. Zhao, X. Li, H. Wu, M. Gao, Q. Wang, D. Li, J. Feng, Rational regulation of spatially adjacent $Al_{4c}$ and $Al_{6c}$ sites assisted Ru catalysts for low-$NH_3$ furfural tandem reductive amination, Chem. Eng. Sci. 258 (2022) 117777.

[16] C. Dong, Y. Wu, H. Wang, J. Peng, Y. Li, C. Samart, M. Ding, Facile and efficient synthesis of primary amines via reductive amination over a Ni/$Al_2O_3$ catalyst, ACS Sustain. Chem. Eng. 9 (2021) 7318–7327.

[17] Y. Yang, L. Zhou, X. Wang, L. Zhang, H. Cheng, F. Zhao, Catalytic reductive amination of furfural to furfurylamine on robust ultra-small Ni nanoparticles, Nano Res. 16 (2023) 3719–3729.

[18] Y. Watanabe, Y. Tsuji, Y. Ohsugi, The ruthenium catalyzed N-alkylation and N-heterocyclization of aniline using alcohols and aldehydes, Tetrahedron Lett. 22 (1981) 2667–2670.

[19] G. Liang, Y. Zhou, J. Zhao, A.Y. Khodakov, V.V. Ordomsky, Structure-sensitive and insensitive reactions in alcohol amination over nonsupported Ru nanoparticles, ACS Catal. 8 (2018) 11226–11234.

[20] L. Fang, Z. Yan, J. Wu, A. Bugaev, C. Lamberti, M. Pera-Titus, Highly selective Ru/HBEA catalyst for the direct amination of fatty alcohols with ammonia, Appl. Catal. B Environ. 286 (2021) 119942.

[21] D.R. Aireddy, K. Ding, Heterolytic dissociation of $H_2$ in heterogeneous catalysis, ACS Catal. 12 (2022) 4707–4723.

[22] I. Cano, L.M. Martínez-Prieto, P.W.N.M. van Leeuwen, Heterolytic cleavage of dihydrogen (HCD) in metal nanoparticle catalysis, Catal. Sci. Technol. 11 (2021) 1157–1185.

[23] A. Nova, D. Balcells, N.D. Schley, G.E. Dobereiner, R.H. Crabtree, O. Eisenstein, An experimental−theoretical study of the factors that affect the switch between ruthenium-catalyzed dehydrogenative amide formation versus amine alkylation, Organometallics 29 (2010) 6548–6558.

[24] M. Tamura, K. Tokonami, Y. Nakagawa, K. Tomishige, Selective hydrogenation of crotonaldehyde to crotyl alcohol over metal oxide modified ir catalysts and mechanistic insight, ACS Catal. 6 (2016) 3600–3609.

[25] G. Skara, F. De Vleeschouwer, P. Geerlings, F. De Proft, B. Pinter, Heterolytic splitting of molecular hydrogen by frustrated and classical Lewis Pairs: a unified reactivity concept, Sci. Rep. 7 (2017) 16024.

[26] Q. Wang, J. Feng, L. Zheng, B. Wang, R. Bi, Y. He, H. Liu, D. Li, Interfacial structure-determined reaction pathway and selectivity for 5-(Hydroxymethyl) furfural hydrogenation over Cu-based catalysts, ACS Catal. 10 (2020) 1353–1365.

[27] Y. Zhang, X. Zhang, P. Yang, M. Gao, J. Feng, D. Li, In situ topologically induced PtZn alloy @ $ZnTiO_x$ and the synergistic effect on glycerol oxidation, Appl. Catal. B Environ. 298 (2021) 120634.

[28] T. Hui, C. Miao, J. Feng, Y. Liu, Q. Wang, Y. Wang, D. Li, Atmosphere induced amorphous and permeable carbon layer encapsulating PtGa catalyst for selective cinnamaldehyde hydrogenation, J. Catal. 389 (2020) 229–240.

[29] D. Zhou, P. Li, X. Lin, A. McKinley, Y. Kuang, W. Liu, W.-F. Lin, X. Sun, X. Duan, Layered double hydroxide-based electrocatalysts for the oxygen evolution reaction: identification and tailoring of active sites, and superaerophobic nanoarray electrode assembly, Chem. Soc. Rev. 50 (2021) 8790–8817.

[30] G. Fan, F. Li, D.G. Evans, X. Duan, Catalytic applications of layered double hydroxides: recent advances and perspectives, Chem. Soc. Rev. 43 (2014) 7040–7066.

[31] Y. Kita, M. Kuwabara, S. Yamadera, K. Kamata, M. Hara, Effects of ruthenium hydride species on primary amine synthesis by direct amination of alcohols over a heterogeneous Ru catalyst, Chem. Sci. 11 (2020) 9884–9890.

[32] D. Deng, Y. Kita, K. Kamata, M. Hara, Low-temperature reductive amination of carbonyl compounds over ru deposited on $Nb_2O_5{\cdot}nH_2O$, ACS Sustain. Chem. Eng. 7 (2019) 4692–4698.

[33] T. Komanoya, T. Kinemura, Y. Kita, K. Kamata, M. Hara, Electronic effect of ruthenium nanoparticles on efficient reductive amination of carbonyl compounds, J. Am. Chem. Soc. 139 (2017) 11493–11499.

[34] X.-P. Fu, P. Han, Y.-Z. Wang, S. Wang, N. Yan, Insight into the roles of ammonia during direct alcohol amination over supported Ru catalysts, J. Catal. 399 (2021) 121–131.

[35] H. Qi, J. Yang, F. Liu, L. Zhang, J. Yang, X. Liu, L. Li, Y. Su, Y. Liu, R. Hao, A. Wang, T. Zhang, Highly selective and robust single-atom catalyst Ru1/NC for reductive amination of aldehydes/ketones, Nat. Commun. 12 (2021) 3295.

[36] K. Wang, C. Miao, Y. Liu, L. Cai, W. Jones, J. Fan, D. Li, J. Feng, Vacancy enriched ultrathin TiMgAl-layered double hydroxide/graphene oxides composites as highly efficient visible-light catalysts for $CO_2$ reduction, Appl. Catal. B Environ. 270 (2020) 118878.

[37] D. Chandra, Y. Inoue, M. Sasase, M. Kitano, A. Bhaumik, K. Kamata, H. Hosono, M. Hara, A high performance catalyst of shape-specific ruthenium nanoparticles for production of primary amines by reductive amination of carbonyl compounds, Chem. Sci. 9 (2018) 5949–5956.

[38] L. Wang, J. Zhang, Y. Zhu, S. Xu, C. Wang, C. Bian, X. Meng, F.-S. Xiao, Strong metal–support interactions achieved by hydroxide-to-oxide support transformation for preparation of sinter-resistant gold nanoparticle catalysts, ACS Catal. 7 (2017) 7461–7465.

[39] J. Mao, W. Chen, W. Sun, Z. Chen, J. Pei, D. He, C. Lv, D. Wang, Y. Li, Rational control of the selectivity of a ruthenium catalyst for hydrogenation of 4-nitro-styrene by strain regulation, Angew. Chem. Int. Ed. 56 (2017) 11971–11975.

[40] X. Li, M. Wang, R. Wang, Y. Wang, M. Zhu, L. Zhang, J. Shi, Construction of ru single-atoms on ceria to reform the products of $CO_2$ photoreduction, ACS Nano 18 (2024) 5741–5751.

[41] H. Shi, Y. Yang, P. Meng, J. Yang, W. Zheng, P. Wang, Y. Zhang, X. Chen, Z. Cheng, C. Zong, D. Wang, Q. Chen, Local charge transfer unveils antideactivation of ru at high potentials for the alkaline hydrogen oxidation reaction, J. Am. Chem. Soc. 146 (2024) 16619–16629.

[42] S. Wang, X. Lan, B. Liu, B. Ali, T. Wang, Boosting amination of 1-octanol to 1-octylamine via metal-metal oxide interactions in $NiFe_1/Al_2O_3$ catalysts, ChemCatChem 14 (2022) e202101728.

[43] A. Tomer, F. Wyrwalski, C. Przybylski, J.-F. Paul, E. Monflier, M. Pera-Titus, A. Ponchel, Facile preparation of Ni/$Al_2O_3$ catalytic formulations with the aid of cyclodextrin complexes: Towards highly active and robust catalysts for the direct amination of alcohols, J. Catal. 356 (2017) 111–124.

[44] A. Tomer, B.T. Kusema, J.-F. Paul, C. Przybylski, E. Monflier, M. Pera-Titus, A. Ponchel, Cyclodextrin-assisted low-metal Ni-Pd/$Al_2O_3$ bimetallic catalysts for the direct amination of aliphatic alcohols, J. Catal. 368 (2018) 172–189.

[45] K.-i Shimizu, K. Kon, W. Onodera, H. Yamazaki, J.N. Kondo, Heterogeneous Ni catalyst for direct synthesis of primary amines from alcohols and ammonia, ACS Catal. 3 (2013) 112–117.

[46] A. Tomer, Z. Yan, A. Ponchel, M. Pera-Titus, Mixed oxides supported low-nickel formulations for the direct amination of aliphatic alcohols with ammonia, J. Catal. 356 (2017) 133–146.

[47] S. Wang, Y. Li, X. Lan, B. Liu, T. Wang, Combining $Ni_3P$ and Lewis acid–base pair as a high-performance catalyst for amination of 1-octanol, Catal. Lett. 153 (2023) 1215–1226.

[48] R.D. Armstrong, J. Hirayama, D.W. Knight, G.J. Hutchings, Quantitative Determination of Pt- Catalyzed d-Glucose Oxidation Products Using $^2$D NMR, ACS Catal. 9 (2019) 325–335.

[49] X. Deng, B. Qin, R. Liu, X. Qin, W. Dai, G. Wu, N. Guan, D. Ma, L. Li, Zeolite-encaged isolated platinum ions enable heterolytic dihydrogen activation and selective hydrogenations, J. Am. Chem. Soc. 143 (2021) 20898–20906.
[50] K. Liu, R. Qin, K. Li, W. Zhang, P. Ruan, G. Fu, N. Zheng, Atomically dispersed palladium catalyzes H/D exchange and isomerization of alkenes via reversible insertion and elimination, Chem. Catal. 1 (2021) 1480–1492.
[51] C. Xie, J. Song, M. Hua, Y. Hu, X. Huang, H. Wu, G. Yang, B. Han, Ambient-temperature synthesis of primary amines via reductive amination of carbonyl compounds, ACS Catal. 10 (2020) 7763–7772.